Composites Part B 318 (2026) 113647

Contents lists available at ScienceDirect

Composites Part B

journal homepage: www.elsevier.com/locate/compositesb

Preliminary design and validation of a hybrid triangular rollable and collapsible boom based on high strain and shape memory polymer composites

Dou Zhang [a], Changyu Shan [b], Fengfeng Li [a,*], Peidong Liu [a], Yin Xing [a], Xin Lan [b], Genyang Cao [c], Liwu Liu [a], Yanju Liu [a,d,**], Jinsong Leng [b]

[a] Department of Astronautical Science and Mechanics, Harbin Institute of Technology, Harbin, 150001, People's Republic of China
[b] Center for Composite Materials and Structures, Science Park of Harbin Institute of Technology, Harbin, 150080, People's Republic of China
[c] State Key Laboratory of New Textile Materials and Advanced Processing Technologies, Wuhan Textile University, Wuhan, Hubei, 430200, People's Republic of China
[d] Suzhou Research Institute, Harbin Institute of Technology, Suzhou, 215100, People's Republic of China

ARTICLE INFO

Keywords:
Aramid-basalt fiber fabric
Shape memory polymer composite
High strain composite
Hybrid composite
Deployable structures

ABSTRACT

Shape memory polymer composites (SMPCs) are attractive for space deployable structures, yet their deployment is often limited by insufficient recovery moment. To address this challenge, this work proposes a bilayer hybrid composite strategy that integrates a high strain composite (HSC) layer with an SMPC layer. In this configuration, the SMPC enables thermally activated self locking and shape recovery, while the HSC serves as an elastic energy storage component to boost actuation. Mechanical characterization under varied thermal conditions shows the SMPC undergoes more pronounced stiffness reduction with increasing temperature while exhibiting greater failure strain compared to the HSC. A basalt-aramid hybrid fabric is employed to improve toughness and provide an ISRU-informed design perspective by increasing the fraction of mineral based reinforcement. Experimental validation confirms that the hybrid structure retains the shape memory capability of SMPCs while significantly increasing the recovery moment. Under constrained displacement recovery with the SMPC thickness fixed at 0.5 mm, increasing the HSC thickness to 0.35 mm raises the normalized recovery moment by 15-fold. Using 18 W electrothermal actuation, the boom achieved deployment with a recovery time of 63 s. Although some discrepancies in transient response were observed between simulations and experiments, mainly due to boundary condition idealization, the model captures the steady-state recovery moment, which is a practically relevant parameter for engineering applications. This study demonstrates that the proposed hybrid composite approach offers a viable pathway to develop high performance self deployable structures that combine substantial recovery moment with commandable thermal actuation.

1. Introduction

Space deployable structures are critical components for modern spacecrafts, enabling large scale platforms such as solar arrays, antennas, and trusses to be stowed compactly during launch and deployed reliably once in orbit [1–3]. The pursuit of higher payload capacity and functionality in satellites and space stations has driven the demand for structures that offer an exceptional stowage to deployment ratio, minimal mass, and high dimensional stability in the harsh space environment. Traditional mechanical deployment mechanisms, while widely used, often involve complex systems of hinges, motors, and latches [4–6]. These systems introduce significant mass, potential failure points, and undesirable shock during deployment. To overcome these limitations, significant research attention has turned to flexible deployable structures based on smart materials, which promise simpler, lighter, and more reliable deployment.

Among various smart materials, shape memory polymers and their composites (SMPCs) have garnered significant attention due to their unique shape memory effects [7,8]. SMPCs can actively recover their original permanent shape from a temporary, deformed state upon

* Corresponding author.
** Corresponding author. Department of Astronautical Science and Mechanics, Harbin Institute of Technology, Harbin, 150001, People's Republic of China.
E-mail addresses: lifengfeng@hit.edu.cn (F. Li), yj_liu@hit.edu.cn (Y. Liu).

https://doi.org/10.1016/j.compositesb.2026.113647
Received 10 November 2025; Received in revised form 6 March 2026; Accepted 24 March 2026
Available online 25 March 2026

exposure to external stimuli such as heat, light, electricity, or magnetic fields. This characteristic makes them ideal candidates for realizing structure actuation integrated systems, thereby greatly simplifying system design, reducing launch mass, and enabling smooth, shock free deployment. Their immense potential has been successfully demonstrated in real world aerospace applications [9–11]. Furthermore, SMPCs have been engineered into various deployable space structures, including hinges, trusses, and antennas, highlighting their practical value [12–16]. In parallel with these structural applications, advanced manufacturing techniques and material engineering strategies have emerged as versatile approaches for enhancing SMPCs. Recent studies have demonstrated the potential of 4D printing in creating fiber reinforced composites [17] and programmable bilayer structures [18]. Furthermore, these technologies have expanded the functional horizons of SMPCs, enabling the creation of magnetically responsive soft robots [19], super-stretchable artificial muscles [20], and nanocomposite-reinforced structures with tailored thermomechanical properties [21], thereby providing additional context for the ongoing development of high performance and programmable SMPC systems relevant to deployable structures. Most recently, progress has been made in developing high performance shape memory systems for broader engineering applications, as highlighted in recent works on advanced shape memory mechanisms and multifunctional composite designs [22–27], which provide additional context on recent advances in shape memory properties and multifunctional integration relevant to deployable structures.

Despite their excellent shape memory performance, the widespread engineering application of SMPCs faces a critical bottleneck: the inherently low modulus of the polymer matrix often results in limited recovery force or moment [28]. This high recovery ratio and low recovery force characteristic fails to meet the mechanical output required for deploying large structures or overcoming joint resistance, severely constraining their use in load bearing and actuation integrated scenarios. To overcome the limitation of insufficient recovery force in SMPCs, researchers have explored various strategies, such as employing continuous fiber reinforcement, optimizing layup designs or designing thin walled structures with complex cross sections [29]. While these methods can enhance recovery force, they often remain confined to a single resin system. This limitation can lead to trade-offs, where improvements in force output may come at the cost of reduced stowage efficiency or a significant increase in actuation energy consumption.

High strain Composites (HSCs) have demonstrated significant potential in space deployable structures due to their high specific stiffness and strength, enabling the generation of substantial recovery forces suitable for deploying large scale systems [3,30,31]. These materials have been successfully implemented in critical aerospace applications, such as support structures for space telescopes [32] and solar array deployment mechanisms on the International Space Station [33]. However, unlike SMPCs, HSCs cannot maintain a fixed stowed configuration autonomously. Moreover, the rapid release of stored strain energy during deployment is often accompanied by considerable shock, which may adversely affect sensitive payloads. Once triggered, the deployment process of HSCs is difficult to control actively, precluding the ability to regulate deployment speed or pause the sequence in response to mission demands. To mitigate such uncontrolled dynamics and achieve precise deployment management, additional active control components, such as motors or damping systems, are often required. While these supplementary mechanisms address the inherent limitations of HSCs in deployment controllability, they also introduce additional complexity, mass, and potential failure points into the system.

Based on the win-win consideration, we propose a hybrid configuration that integrates HSC layers with SMPC layers to create a multifunctional actuator structure component. In this architecture, the SMPC serves as the actuation source, responding to thermal stimuli to frozen packaged state and initiate shape recovery, while the HSC functions as an elastic energy reservoir that stores substantial strain energy during deformation and releases it cooperatively during thermal activation, thereby substantially amplifying the total recovery force. Following this design concept, a hybrid triangular rollable and collapsible (TRAC) boom was proposed. This work comprehensively analyzes the mechanical properties of the TRAC boom and systematically examines its thermomechanical behavior under varying boundary conditions. Additionally, a basalt-aramid hybrid fabric was employed as the reinforcement material, representing a strategic alternative to conventional carbon fiber composites [34]. This selection gains validation from China's recent Chang'e−6 lunar mission, where similar hybrid fibers demonstrated exceptional durability in the extreme lunar environment. The choice is further motivated by an in-situ resource utilization (ISRU) informed perspective, in which mineral-based reinforcement such as basalt is considered a candidate for regolith derived mineral feedstock, while the polymeric aramid component remains an imported constituent in the present hybrid system. The work conclusively validates the efficacy of the hybrid design in achieving both high shape recovery ratio and enhanced recovery moment, offering valuable insights for the development of advanced deployable space structures.

2. Design and analysis of the TRAC hybrid boom

2.1. The concept of the TRAC hybrid boom

The TRAC boom in Fig. 1(a) employs an open section design, consisting of two circular arc flanges connected via a flat web. It exhibits a symmetrical layout about the bending axis, rendering the moment rotation relationship independent of the folding direction. The TRAC boom is hybridized by an additional SMPC layer in the flange region of a typical HSC based configuration, achieving enhanced adaptive deformation. This modification leverages composite material engineering principles, where functional layers are strategically integrated into structural components to enable stimuli responsive behavior. Specifically, as shown in Fig. 1(b), the flange region, a critical stress concentration zone, was selected for localized reinforcement and actuation tuning. Its structural configuration is governed by four key design parameters:

Transverse curvature radius (*R*) - defining the arc geometry of the cross section;

Thickness (*t*) - including the thickness of HSC layer (t_1) and SMPC layer (t_2), determining bending stiffness and energy storage capacity;

Opening angle (φ) - describing the angular separation between unconstrained flange ends;

Web segment width (*w*) - controlling the effective contact area at the joining interface.

2.2. Theoretical bending moment

The triangular configuration enables deformation adaptability in the cross sectional direction. When compressed, the boom can be flattened and coiled for compact storage, while restoring its original cross sectional shape provides sufficient stiffness. To analyze the pure bending moment characteristics, a strain energy mathematical model was established based on the von Kármán large deflection theory of thin plates. The model focuses on quantifying the strain energy under pure bending conditions. The theoretical framework considers the geometric nonlinearity induced by significant deformations, aligning with strain load relationships observed in experimental studies. The total energy of the system can be divided into two parts: the energy in web and the energy in flanges. Further, bending approaches of flanges include opposite-sense bending and equal-sense bending. A coordinate system is established in the flange section of the TRAC boom, as illustrated in Fig. 2(b).

The flange can be denoted as:

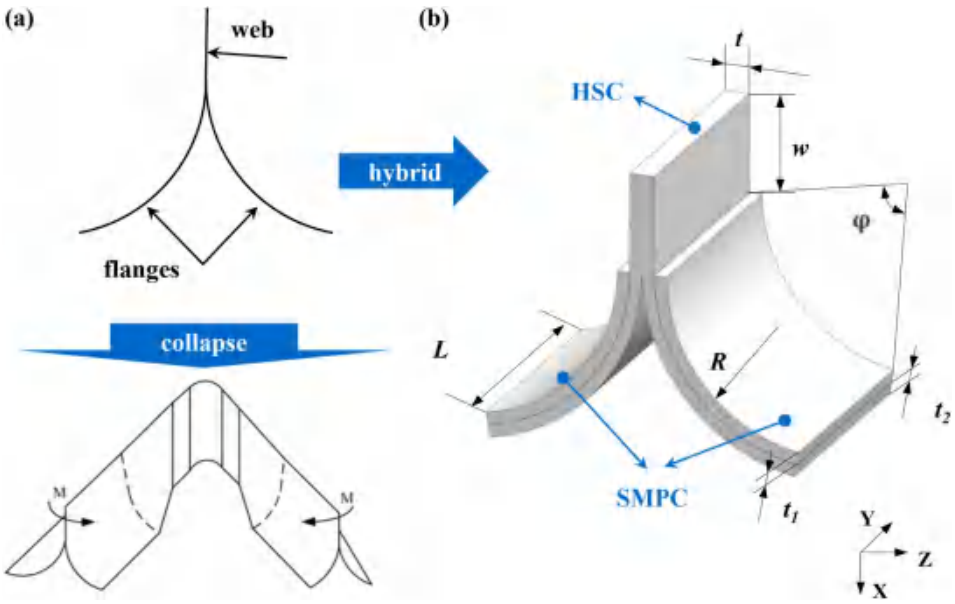

Fig. 1. The hybrid TRAC boom, (a) typical configuration and (b) hybrid strategy.

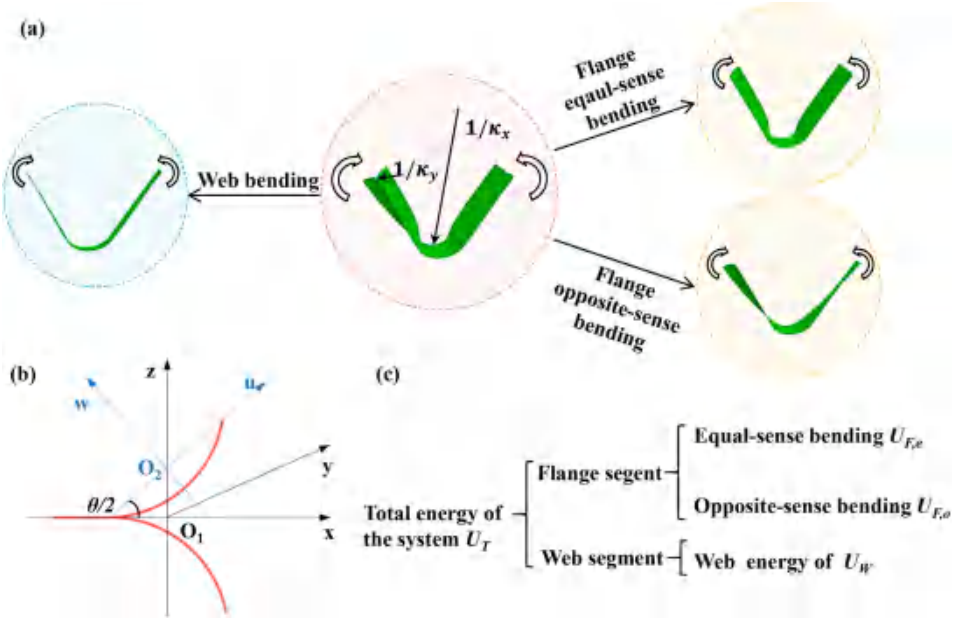

Fig. 2. The folded TRAC boom, (a) deformation characteristics, (b) coordinate system of cross section and (c) energy composition.

$$u = \frac{y}{\cos\frac{\varphi}{2}} \tag{1}$$

The deflection w of the flange is analytically derived as:

$$w_y = c_1 \sin h\frac{y}{n\cos\frac{\varphi}{2}}\sin\frac{y}{n\cos\frac{\varphi}{2}} + c_2 \cos h\frac{y}{n\cos\frac{\varphi}{2}}\cos\frac{y}{n\cos\frac{\varphi}{2}} \tag{2}$$

where,

$$\begin{cases} c_1 = \dfrac{n^2}{2}\left(\Delta\kappa_x - \dfrac{1}{R}\right)\dfrac{\sin h\frac{b}{2n}\cos\frac{b}{2n} + \cos h\frac{b}{2n}\sin\frac{b}{2n}}{\sin h\frac{b}{2n}\cos h\frac{b}{2n} + \sin\frac{b}{2n}\cos\frac{b}{2n}} \\ c_2 = \dfrac{n^2}{2}\left(\Delta\kappa_x - \dfrac{1}{R}\right)\dfrac{\sin h\frac{b}{2n}\cos\frac{b}{2n} - \cos h\frac{b}{2n}\sin\frac{b}{2n}}{\sin h\frac{b}{2n}\cos h\frac{b}{2n} + \sin\frac{b}{2n}\cos\frac{b}{2n}} \\ b = 2R\sin\dfrac{\varphi}{2} \end{cases} \tag{3}$$

Since the flange is not subjected to loading along the y axis, the transverse strain in the neutral plane along the y direction remains zero. However, the longitudinal strain in the neutral plane is given by:

$$\begin{cases} \varepsilon_x = \kappa_x w_y \\ \varepsilon_y = 0 \end{cases} \tag{4}$$

The initial longitudinal curvature along the x axis is $\kappa_{x,0} = 0$, and the initial transverse curvature along the y axis can be expressed as $\kappa_{y,0} = 1/R$. When the shell deforms, the transverse curvature becomes:

$$\kappa_y = \pm \frac{d^2 w_y}{du^2} \tag{5}$$

where the positive and negative signs indicate equal-sense bending and opposite sense bending, respectively. The constitutive equations in the neutral plane of the flange can be expressed as:

$$\begin{cases} N_x = A_{11}\varepsilon_x + A_{12}\varepsilon_y \\ M_x = D_{11}\Delta\kappa_x + D_{12}\Delta\kappa_y \\ M_x = D_{12}\Delta\kappa_x + D_{22}\Delta\kappa_y \end{cases} \tag{6}$$

where $\Delta\kappa_x$ and $\Delta\kappa_y$ represent the changes in curvature along the x and y directions in the neutral plane, respectively. Specifically:

$$\begin{cases} \Delta\kappa_x = \kappa_x \\ \Delta\kappa_y = \pm\dfrac{d^2 w_y}{du^2} - 1 \Big/ R \end{cases} \tag{7}$$

Assuming that the curvature variations in x and y directions of the shell are uniformly distributed across any position during bending deformation, the strain energy under pure bending conditions comprises two components: tensile strain energy U_t generated by the stretching strain at the neutral surface, and bending strain energy U_b arising from transverse and longitudinal curvature changes. These two energies can be calculated as:

$$\begin{cases} U_t = \dfrac{1}{2}\displaystyle\int_{-\frac{b}{2}}^{\frac{b}{2}} \begin{bmatrix} \varepsilon_x & \varepsilon_y & \gamma_{xy} \end{bmatrix} A \begin{bmatrix} \varepsilon_x \\ \varepsilon_y \\ \gamma_{xy} \end{bmatrix} du \\ U_b = \dfrac{1}{2}\displaystyle\int_{-\frac{b}{2}}^{\frac{b}{2}} \begin{bmatrix} M_x & M_y & M_{xy} \end{bmatrix} A \begin{bmatrix} \Delta\kappa_x \\ \Delta\kappa_y \\ \Delta\kappa_z \end{bmatrix} du \end{cases} \tag{8}$$

Substituting Eqs (4), (6) and (7) into Eq (8), the tensile and bending energies of the flange can be derived as:

$$\begin{cases} U_t = \dfrac{1}{2}\displaystyle\int_{-\frac{b}{2}\cos\varphi}^{\frac{b}{2}\cos\varphi} A_{11}{\kappa_x}^2 {w_y}^2 dy \\ U_b = \dfrac{1}{2}\left(D_{11}{\kappa_x}^2 - 2\dfrac{D_{12}\kappa_x}{R} + \dfrac{D_{22}}{R^2}\right)b + \dfrac{1}{4}D_{22}\displaystyle\int_{-\frac{b}{2}\cos\varphi}^{\frac{b}{2}\cos\varphi} {\kappa_y}^2 dy + \left(D_{12}\kappa_x - \dfrac{D_{22}}{R}\right)\int_{-\frac{b}{2}\cos\varphi}^{\frac{b}{2}\cos\varphi} \kappa_y dy \end{cases} \tag{9}$$

Plug Eq (2) into (9), the strain energy of flange in equal-sense bending $U_{F,e}$ can be calculated as:

$$U_{F,e} = U_t + U_b = \frac{D_{22}{\xi_1}^2 R\kappa_x n}{16\cos\frac{\varphi}{2}}\left[2\lambda_1\lambda_2\delta_2 + {\lambda_2}^2(2\eta_1+\delta_1) + {\lambda_1}^2(2\eta_2-\delta_1)\right] + \frac{D_{22}{\xi_1}^2 n^5}{64\cos\frac{\varphi}{2}}\Big[- 2\lambda_1\lambda_2\delta_2 + {\lambda_2}^2(2\eta_1-\delta_1) + {\lambda_1}^2(2\eta_2+\delta_1)\Big] + \frac{1}{2\cos\frac{\varphi}{2}}\left(D_{11}{\kappa_x}^2 - \frac{2D_{12}\kappa_x}{R} + \frac{D_{22}}{R^2}\right)b + \frac{1}{\cos\frac{\varphi}{2}}D_{22}{\xi_1}^2 n\left({\lambda_1}^2 + {\lambda_2}^2\right)\tau_1 \tag{10}$$

The strain energy of the flange in opposite-sense bending $U_{F,o}$ can be derived as:

$$U_{F,o} = = -\frac{D_{22}{\xi_2}^2 R\kappa_x n}{16\cos\frac{\varphi}{2}}\left[2\lambda_1\lambda_2\delta_2 + {\lambda_2}^2(2\eta_1+\delta_1) + {\lambda_1}^2(2\eta_2-\delta_1)\right] + \frac{D_{22}{\xi_2}^2 n^5}{64\cos\frac{\varphi}{2}}\Big[- 2\lambda_1\lambda_2\delta_2 + {\lambda_2}^2(2\eta_1-\delta_1) + {\lambda_1}^2(2\eta_2+\delta_1)\Big] + \frac{1}{2\cos\frac{\varphi}{2}}\left(D_{11}{\kappa_x}^2 + \frac{2D_{12}\kappa_x}{R} + \frac{D_{22}}{R^2}\right)b + \frac{1}{\cos\frac{\varphi}{2}}D_{22}{\xi_2}^2 n\left({\lambda_1}^2 + {\lambda_2}^2\right)\tau_1 \tag{11}$$

Based on the analysis of flanges, bending energy of the web segment is deduced by the analogous method:

$$U_w = \frac{1}{2\cos\frac{\varphi}{2}}\left(D_{11}{}^T\kappa_x{}^2 - \frac{2D_{12}{}^T\kappa_x}{R} + \frac{D_{22}{}^T}{R^2}\right)a + \frac{1}{\cos\frac{\varphi}{2}}D_{22}{}^T\xi_1{}^2 n_1\left(\lambda_3{}^2+\lambda_4{}^2\right)\tau_2 + \frac{D_{22}{}^T\xi_1{}^2 n_1{}^5}{64\cos\frac{\varphi}{2}}\left[-2\lambda_3\lambda_4\delta_4 + \lambda_3{}^2(2\eta_4+\delta_3) + \lambda_4{}^2(2\eta_3-\delta_3)\right]$$
$$+ \frac{D_{22}\xi_1{}^2 R\kappa_x n_1}{16\cos\frac{\varphi}{2}}\left[2\lambda_3\lambda_4\delta_4 + \lambda_3{}^2(2\eta_3+\delta_3) + \lambda_4{}^2(2\eta_4-\delta_3)\right] \quad (12)$$

where, $\xi_1{}^2 = \left(\Delta\kappa_x - \frac{1}{R}\right)^2$; $\xi_2{}^2 = \left(-\Delta\kappa_x - \frac{1}{R}\right)^2$; $a = 2R\sin\frac{\alpha}{2}$; $n_1 = \left[\frac{4D_{22}{}^T R}{A_{11}{}^T\kappa_x}\right]^{\frac{1}{4}}$; $\eta_1 = \frac{b}{n} + \sin h\frac{b}{n} + \sin\frac{b}{n}$; $\eta_2 = -\frac{b}{n} + \sin h\frac{b}{n} + \sin\frac{b}{n}$; $\eta_3 = \frac{a}{n_1} + \sin h\frac{a}{n_1} + \sin\frac{a}{n_1}$; $\delta_1 = \cos\frac{b}{n}\sin\frac{b}{n} + \sin h\frac{b}{n}\cos h\frac{b}{n}$; $\delta_2 = \cos\frac{b}{n}\sin\frac{b}{n} - \sin h\frac{b}{n}\cos h\frac{b}{n}$; $\delta_3 = \cos\frac{a}{n_1}\sin\frac{a}{n_1} + \sin h\frac{a}{n_1}\cos h\frac{a}{n_1}$; $\delta_4 = \cos h\frac{b}{n_1}\sin\frac{b}{n_1} + \sin h\frac{b}{n_1}\cos h\frac{b}{n_1}$; $\tau_1 = \sin h\frac{b}{2n}\cos h\frac{b}{2n} + \sin\frac{b}{2n}\cos\frac{b}{2n}$; $\tau_2 = \sin h\frac{a}{2n_1}\cos h\frac{a}{2n_1} + \sin\frac{a}{2n_1}\cos\frac{a}{2n_1}$.

The total strain energy can be described as:

$$U_T = U_{F,e} + U_{F,o} + U_w \quad (13)$$

Under the assumption that the TRAC boom undergoes uniform and homogeneous deformation throughout the bending deformation, the bending moment per unit length can be derived using the principle of minimum potential energy:

$$M = \frac{\partial U_T}{\partial\kappa_x} \quad (14)$$

It should be emphasized that while the stiffness matrices [A] and [D] in the preceding analysis employ identical mathematical representations for notational simplification, each component in practical engineering designs may incorporate heterogeneous material combinations. Consequently, the explicit formulation of these stiffness matrices will exhibit material specific variations. The derivation of bending moment proves analytically intractable due to coupled anisotropic terms and higher order curvature dependencies. To circumvent these computational limitations while ensuring solution fidelity, a finite element methodology will subsequently be implemented to obtain numerical resolution.

2.3. Material preparation and characterization

Two types of epoxy resins from Jinsong Leng's group were employed as the composite matrix: a conventional epoxy resin for the prepreg constituting the HSC layer, and a functional shape memory epoxy resin serving as the SMPC layer. Given that both matrices are compatible epoxy based systems, the bilayer laminate was fabricated by co-curing to promote intrinsic chemical continuity at the HSC-SMPC interface. The latter has achieved successful implementation in both Earth orbital operations and Tianwen-1 Mars exploration endeavors. The aramid-basalt fiber fabric is from Weilin Xu's group, which was woven in a 2/1 twill pattern using aramid and basalt yarns, each with a linear density of 8.8 tex (50 filaments per bundle).

The HSC coupons was subjected to a curing cycle, involving 180 °C heating for 2 h with a heating rate of 0.5 °C/min. During the curing process, a controlled pressure of 0.4 atm was applied to ensure proper resin flow, minimize void formation, and enhance interfacial bonding between the fiber reinforcement and the epoxy matrix. The SMPC is fabricated through Vacuum Assisted Resin Infusion (VARI) technology, of which the detailed fabrication process was illustrated in the literature [35]. In order to investigate the mechanical parameters such as modulus and strength, these two kinds of composites were tested by dynamic mechanical analysis (DMA), tensile tests, three-point bending tests, both along warp and weft directions. Here, the basalt fiber orientation is

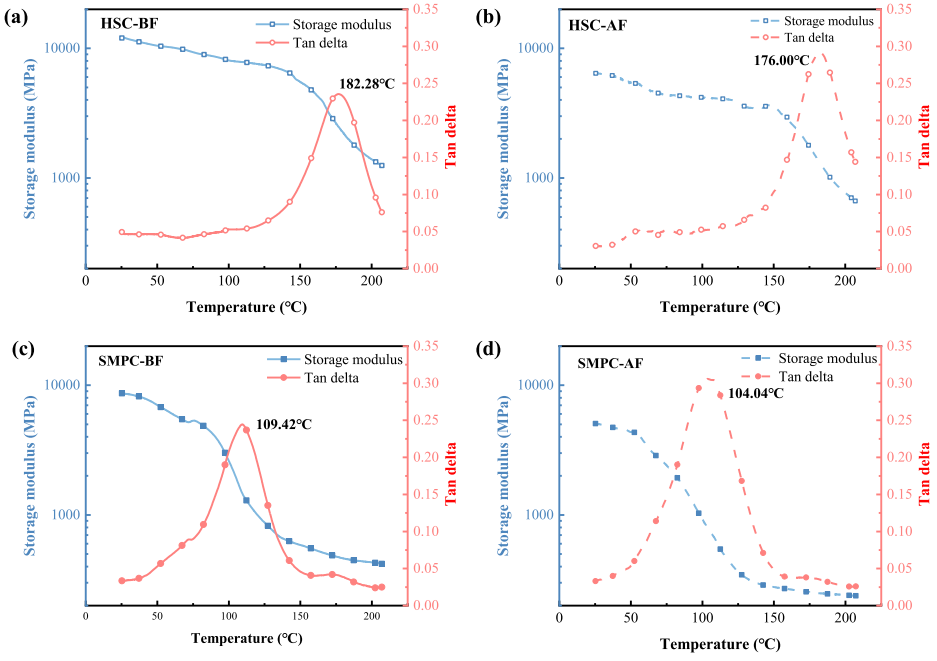

Fig. 3. Storage modulus and tan delta for (a) HSC-BF, (b) HSC-AF, (c) SMPC-BF and (d) SMPC-AF.

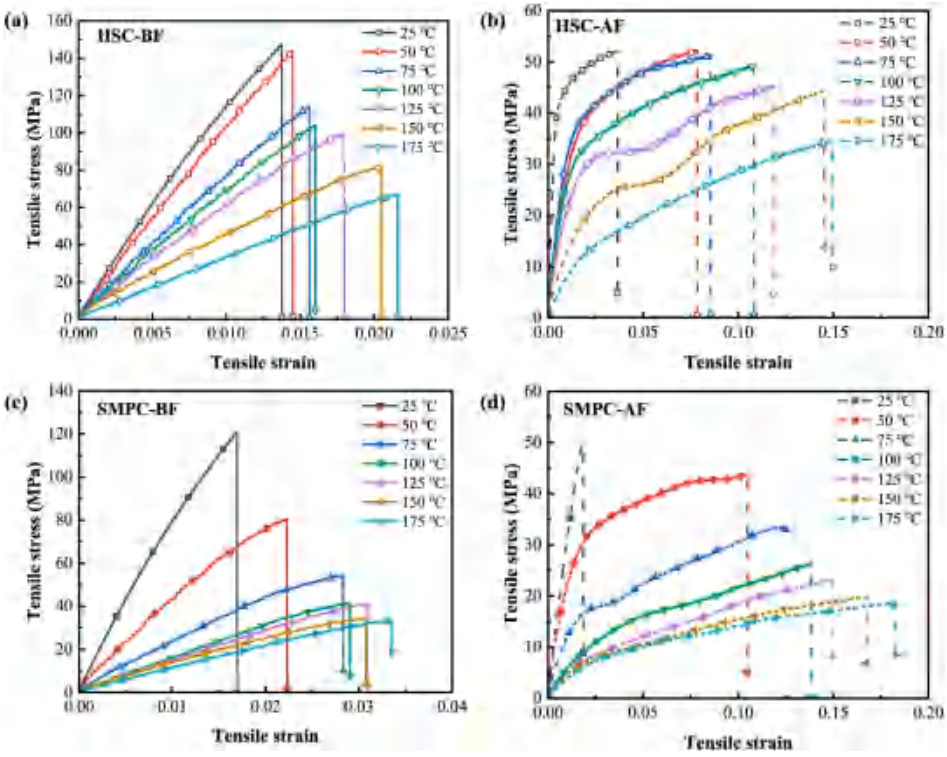

Fig. 4. Tensile stress versus strain curves at different temperatures for HSCs, (a) along BF direction and (b) AF direction; for SMPCs, (c) along BF direction and (d) AF direction.

explicitly defined as the BF direction, while the aramid fiber alignment is designated as the AF direction. The specimens are classified into four groups: HSC-BF, HSC-AF, SMPC-BF, SMPC-AF, where the first denote the composite type and the second represents loading direction. All above experiments were performed in triplicate under controlled humidity conditions (RH 50% ± 5%).

2.3.1. *Dynamic mechanical analysis*

Dynamic mechanical behavior of the composites was characterized using a dynamic mechanical analyzer (TA Q800, three-point bending configuration) with temperature sweep from ambient to 200 °C. Specimens with dimensions of 60 × 12 × 2 mm^3 were preconditioned at 25 °C for 5 min before initiating thermal scans at 3 °C/min. A fixed oscillatory frequency of 1 Hz with 15 μm displacement amplitude was maintained

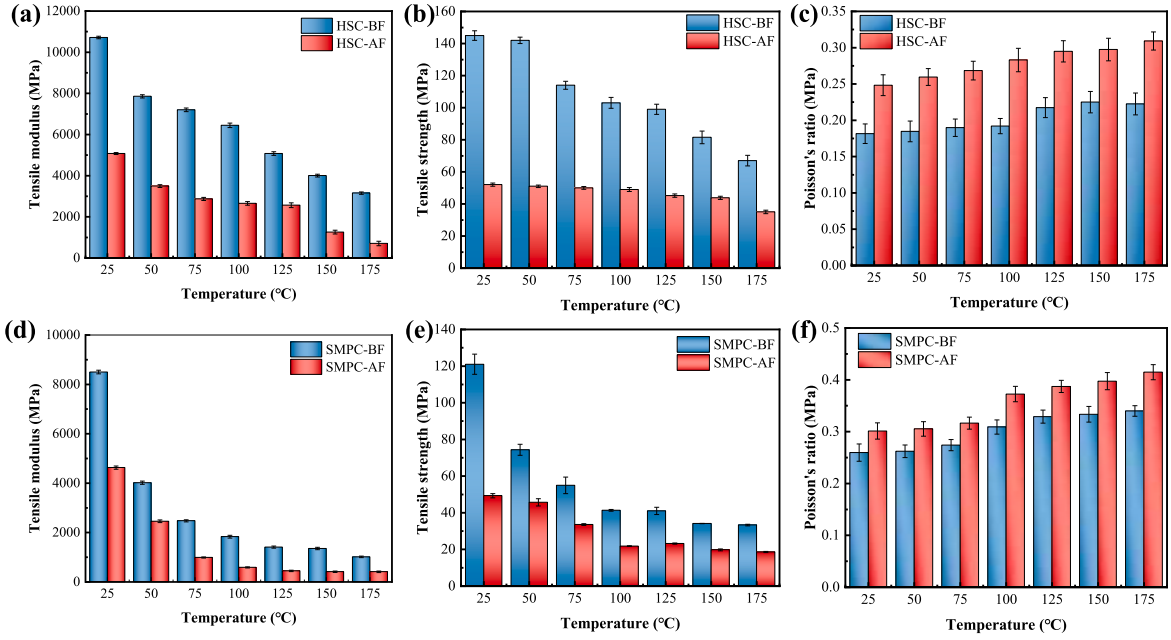

Fig. 5. Tensile mechanical properties at different temperatures, (a) modulus, (b) strength and (c) Poisson's ratio for HSCs; (d) modulus, (e) strength and (f) Poisson's ratio for SMPCs.

throughout the experiment to simultaneously monitor the evolution of storage modulus and loss modulus. The storage modulus and tan delta are shown in Fig. 3. Both HSC and SMPC samples exhibit three characteristic regions: the glassy state, glass transition region, and rubbery state, accompanied by a marked decrease in stiffness with increasing temperature. However, the decline in the storage modulus of the SMPC is significantly more pronounced than that of the HSC, which is a direct manifestation of its shape memory characteristics. The storage modulus in the BF direction was higher than that in the AF direction. Specifically, the glassy state storage moduli of HSC and SMPC in the BF direction reach 12.01 GPa and 8.64 GPa, respectively, compared to 6.41 GPa and 5.06 GPa in the AF direction. This disparity originates from the inherently higher elastic modulus of BF relative to AF. The loss tangent, defined as the ratio of loss modulus to storage modulus, displays an initial increase followed by a decrease with temperature. The peak values are markedly higher in the AF direction (0.293 for HSC and 0.306 for SMPC) than in the BF direction (0.235 for HSC and 0.246 for SMPC), indicating superior damping performance of AF reinforced composites. This enhancement arises from the inherent toughness of AF and viscoelastic frictional energy dissipation at fiber matrix interfaces. In contrast, the high rigidity and dense interfacial structure of BF restrict energy dissipation pathways. The peak tan delta temperatures, corresponding to the T_g, reveal distinct trends. The BF direction exhibited higher T_g compared to the AF direction. This divergence is closely associated with thermal conductivity differences between fibers. The low thermal conductivity of BF (~0.04 W/m·K) delays heat transfer to the resin matrix, resulting in an elevated apparent T_g. Conversely, the higher thermal conductivity of AF (~0.14 W/m·K) facilitates faster resin phase transitions, leading to lower measured values.

2.3.2. Tensile tests

Tensile tests were conducted in accordance with ASTM D3039 standard using a universal testing machine (LE5105, Shanghai LiShi) equipped with a telecentric lens video extensometer (LVE801C) for non contact strain measurement. Prior to testing, the specimens were conditioned for 20 min at the target temperatures (25, 50, 75, 100, 125, 150, 175 °C) to achieve thermal stability. A constant crosshead speed of 2 mm/min with a 5 N preload was applied to ensure quasi static loading conditions. The video extensometer provided high resolution displacement data with a resolution of ±1 μm, enabling accurate determination of strain. The tensile stress versus strain curves in Fig. 4 reveal that the material nonlinearity intensifies with increasing temperature, accompanied by a significant reduction in the slope of the curves. SMPCs exhibit significantly greater modulus degradation compared to HSCs. BF oriented composites demonstrate nearly linear stress-strain responses followed by brittle fracture, while AF oriented specimens exhibit a distinct three stages deformation pattern: initial linear elasticity, prolonged yield plateau, and subsequent strain hardening with enhanced plastic deformation capacity. Fracture strain shows temperature-dependent enhancement, with AF oriented systems at 100 °C achieving 13.78% elongation at break (SMPC-AF) versus 2.9% for BF oriented counterparts (SMPC-BF). This behavioral dichotomy originates from fundamentally distinct failure mechanisms. The hierarchical microfibril architecture of aramid fibers enables sequential energy dissipation through progressive fiber rupture, interfacial debonding, and frictional sliding, thereby delaying catastrophic failure. In contrast, the inherent brittleness combined with strong interfacial adhesion of basalt fibers restrict the plasticity of the matrix, resulting in abrupt fracture without observable yielding.

As shown in Fig. 5, both tensile modulus and strength decrease monotonically with temperature, with SMPCs showing greater sensitivity than HSCs. For example, at 100 °C, the tensile modulus of SMPC-BF is 1.83 GPa, while that of HSC-BF is 7.10 GPa. This behavior correlates directly with T_g disparity of resin matrices. The lower T_g of SMPCs accelerates resin softening and interfacial stress transfer inefficiency at elevated temperatures. At 100 °C, SMPCs exhibit pronounced anisotropy in mechanical properties. The AF oriented composites demonstrate a modulus of 0.58 GPa, representing only 31.69% of their BF oriented counterparts (1.83 GPa). Similarly, the tensile strength of AF oriented systems reached 21.8 MPa, approximately half the value observed in BF oriented specimens (41.33 MPa). These discrepancies arise from higher elastic modulus of basalt fibers and premature debonding in aramid

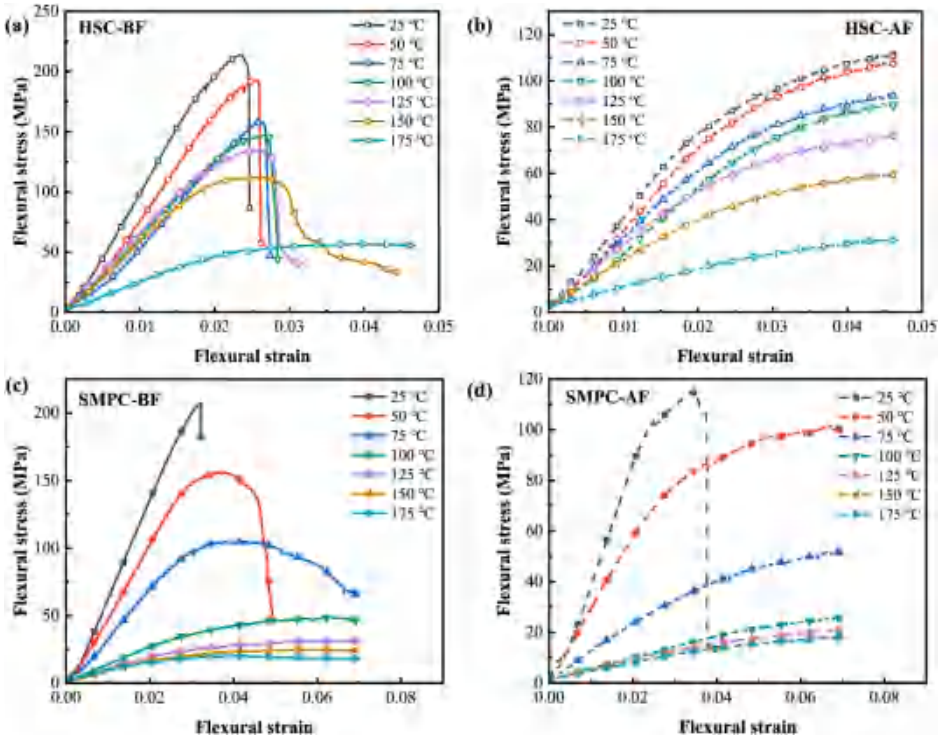

Fig. 6. Flexural stress versus strain curves at different temperatures for HSCs, (a) along BF and (b) AF directions; for SMPCs, (c) along BF and (d) AF directions.

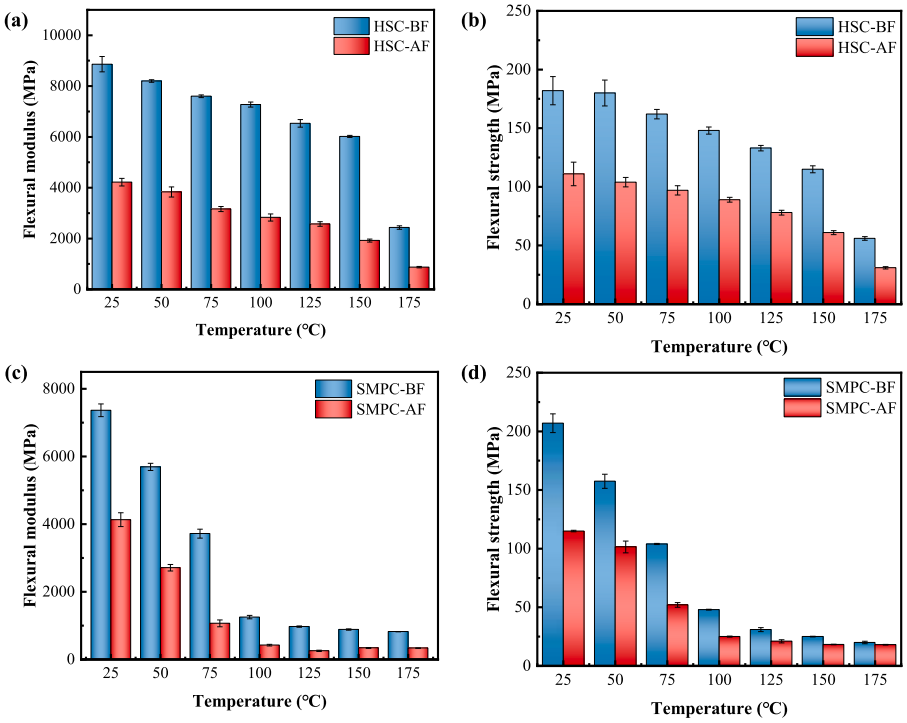

Fig. 7. Bending mechanical properties at different temperatures, (a) flexural modulus and (b) strength for HSCs; (c) flexural modulus and (d) strength for SMPCs.

fibers induced by weaker interfacial shear strength. The Poisson's ratio increases with temperature, particularly near the T_g. This trend originates from enhanced molecular chain mobility in the resin matrix at elevated temperatures, which promotes transverse deformation. The systematically higher Poisson's ratio of SMPC compared to HSC is attributed to the softening of rubbery soft segments in the shape memory epoxy, facilitating chain slippage and volumetric relaxation. Furthermore, the anisotropic compression modulus of aramid fibers amplifies transverse contraction, resulting in higher Poisson's ratios in the AF direction than in the BF direction.

2.3.3. *Three-point bending tests*

The mechanical behavior of the TRAC boom is primarily governed by bending curvature, necessitating three-point bending characterization. Rectangular specimens with a dimension of 12.7 mm in width and 50.8 mm in length were machined in compliance with ASTM D790 specifications. Experiments were carried out on a Zwick/Rolle 010 universal test machine with a 1 kN load cell. The fixture incorporated cylindrical components with 10 mm diameters for both the indenter and support rollers. Following ASTM D790 standards, for samples whose thickness are less than 1.6 mm, the support span is 25.4 mm. A thermal chamber with operational range of −80 to 250 °C was employed to achieve target temperatures at a heating rate of 3 °C/min. To ensure uniform thermal equilibrium, specimens were isothermally stabilized at target temperatures for 20 min prior to mechanical loading. The bending test consisted of a preloading stage at 2 mm/min under a 2 N axial force, followed by the formal test at 1 mm/min. Termination criteria included specimen fracture or attainment of the predefined flexural deflection of 5 mm. The three-point bending test results in Fig. 6 demonstrate a temperature-dependent reduction in the slope of flexural stress-strain curves, though the two materials exhibit distinct trends. For HSCs, the reduction in slope is marginal below 150 °C, beyond which it becomes markedly more pronounced. This behavior further confirms the ability of HSCs to maintain relatively stable stiffness under varying thermal conditions in space. In contrast, the SMPCs show a sharp decline in slope with initial temperature rise, followed by a significantly slowed reduction above 100 °C. This trend reflects the pronounced variable stiffness characteristics inherent to the shape recovery process. Fracture modes exhibit distinct orientation dependence. In BF direction, brittle fracture dominates below 150 °C, transitioning to ductile deformation at elevated temperatures, eventually remaining intact at 175 °C. In AF orientation, except for SMPC-AF fracturing at 25 °C, all other samples retain structural integrity, demonstrating exceptional flexural toughness. The fracture of SMPC-AF at 25 °C originates from the low temperature brittleness of shape memory epoxy's glassy hard segments and interfacial thermal residual stresses, which induce premature interfacial cracking.

As shown in Fig. 7, both flexural modulus and strength decrease monotonically with temperature, with SMPCs showing greater sensitivity than HSCs. For instance, at 100 °C, the modulus of SMPC-BF drops sharply from 7.365 GPa to 1.251 GPa, whereas HSC-BF decreases moderately from 8.861 GPa to 7.271 GPa. This behavior correlates with the significantly lower T_g of SMPC resin, which accelerates segmental relaxation and weakens fibe matrix interface stress transfer at lower temperatures. The AF oriented composites consistently exhibited less than 50% of the flexural modulus of BF oriented systems. For instance, the flexural modulus of HSC-AF at 25 °C is 4.219 GPa, while HSC-BF is 8.861 GPa. However, their strength marginally exceeded 50% of BF values. The flexural strength of HSC-AF at 25 °C is 111 MPa, while HSC-BF is 181 MPa. This discrepancy originates from three synergistic mechanisms. Firstly, the inherently higher elastic modulus of basalt fibers predominantly dictates composite stiffness. Then, energy dissipation through aramid fiber fibrillation and progressive interfacial debonding in AF oriented composites delays crack propagation, thereby maintaining favorable strength to modulus ratios. Finally, brittle interface coupling in BF oriented systems, where strong fiber matrix bonding synchronizes modulus strength degradation through catastrophic basalt fiber fracture.

2.3.4. *Interfacial adhesion and cyclic thermomechanical durability*

The structural integrity and reliability of the hybrid TRAC boom fundamentally depend on the interfacial bonding between the HSC and

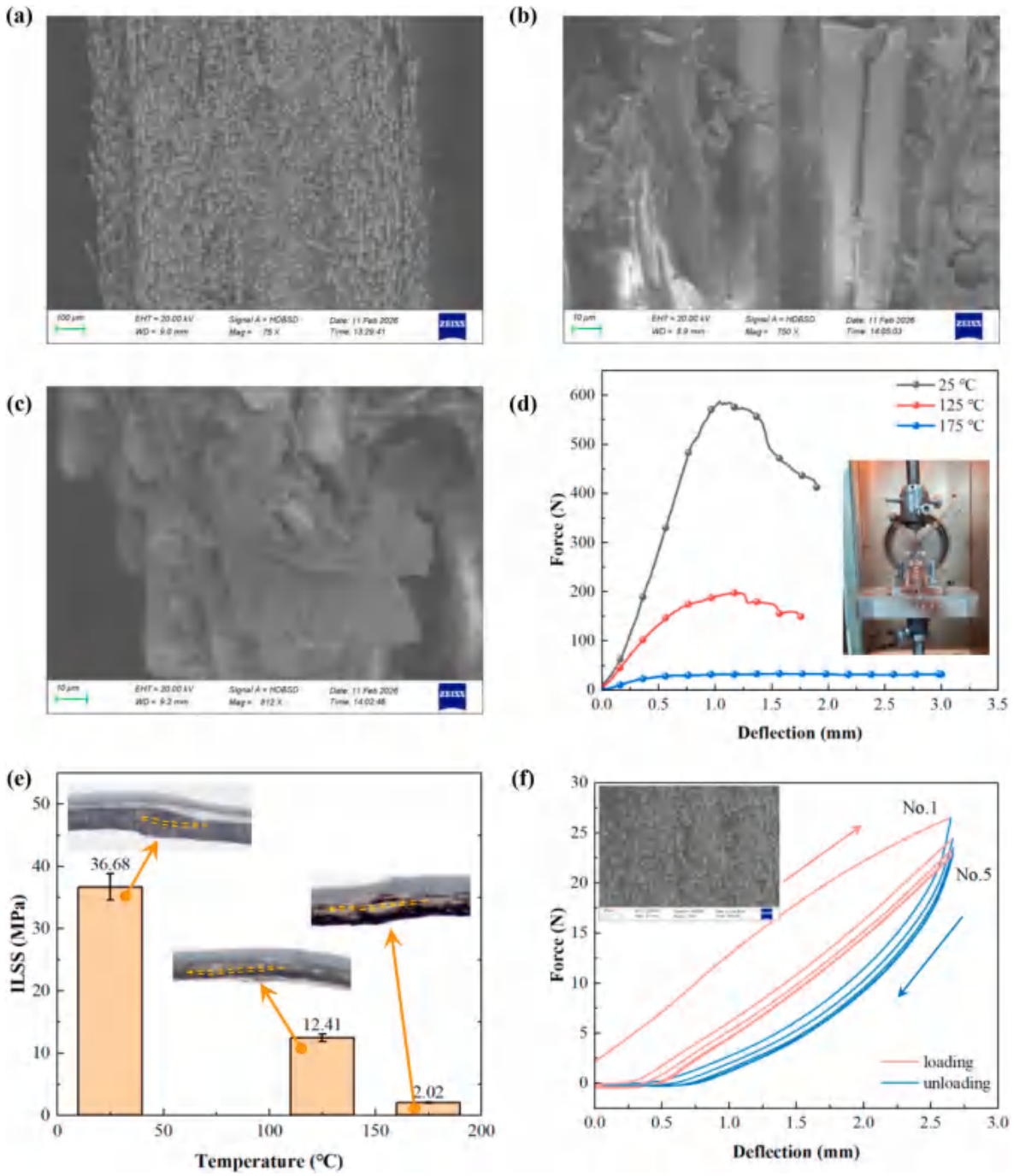

Fig. 8. Interfacial characterization and cyclic thermomechanical properties, (a) SEM image of the HSC-SMPC heterojunction; (b) fiber matrix interface for basalt fibers and (c) aramid fibers; (d) force deflection curves and (e) ILSS results of the hybrid composites at different temperatures; (f) cyclic force versus deflection curves at 125 °C.

Fig. 9. Finite element model of the TRAC boom.

SMPC layers. Since both matrices consist of compatible epoxy based systems, the bilayer structure was fabricated via a co-curing process, facilitating intrinsic chemical bonding at the heterojunction.The microscopic morphology of the interface was characterized using a ZEISS Scanning Electron Microscope (SEM). As shown in Fig. 8(a), the macro interface between the HSC and SMPC layers is dense and continuous, with no detectable macroscopic delamination or cracks. Higher magnification images of the basalt fiber (Fig. 8(b)) and aramid fiber (Fig. 8(c)) regions demonstrate that the resin has thoroughly infiltrated the fiber bundles. The fibers are tightly embedded within the matrix with no observable circumferential gaps or interfacial debonding at the cross section, confirming excellent wetting and strong fiber matrix adhesion. This robust bonding is attributed to the synchronized curing of the shared epoxy backbone, ensuring efficient stress transfer across the heterojunction. To quantitatively evaluate the interfacial strength, Short Beam Shear (SBS) tests were conducted following ASTM D2344. Specimens (width $b = 1.27$ mm, thickness $h = 1.5$ mm) were tested with a

span-to-thickness ratio of 4:1. The tests were performed with a 2 N preload at a rate of 1 mm/min. The interlaminar shear strength (F^{sbs} or ILSS) is calculated as:

$$F^{sbs} = 0.75 \times \frac{P_m}{b \times h} \tag{15}$$

where P_m represents the maximum observed load. As shown in Fig. 8(d) and (e), the interfacial strength is highly sensitive to temperature. The ILSS measured 36.68 MPa at 25 °C, decreasing to 12.41 MPa at125 °C, and further dropping to 2.02 MPa at 175 °C. The inset failure photographs in Fig. 8(e) confirm that the specimens underwent typical interlaminar shear failure which is indicated by the dashed lines, proving that the interface remains structurally integrated until the shear limit of the resin system is reached.

To assess the durability for space applications involving multiple deployment cycles, cyclic three-point bending tests (ASTM D790) were

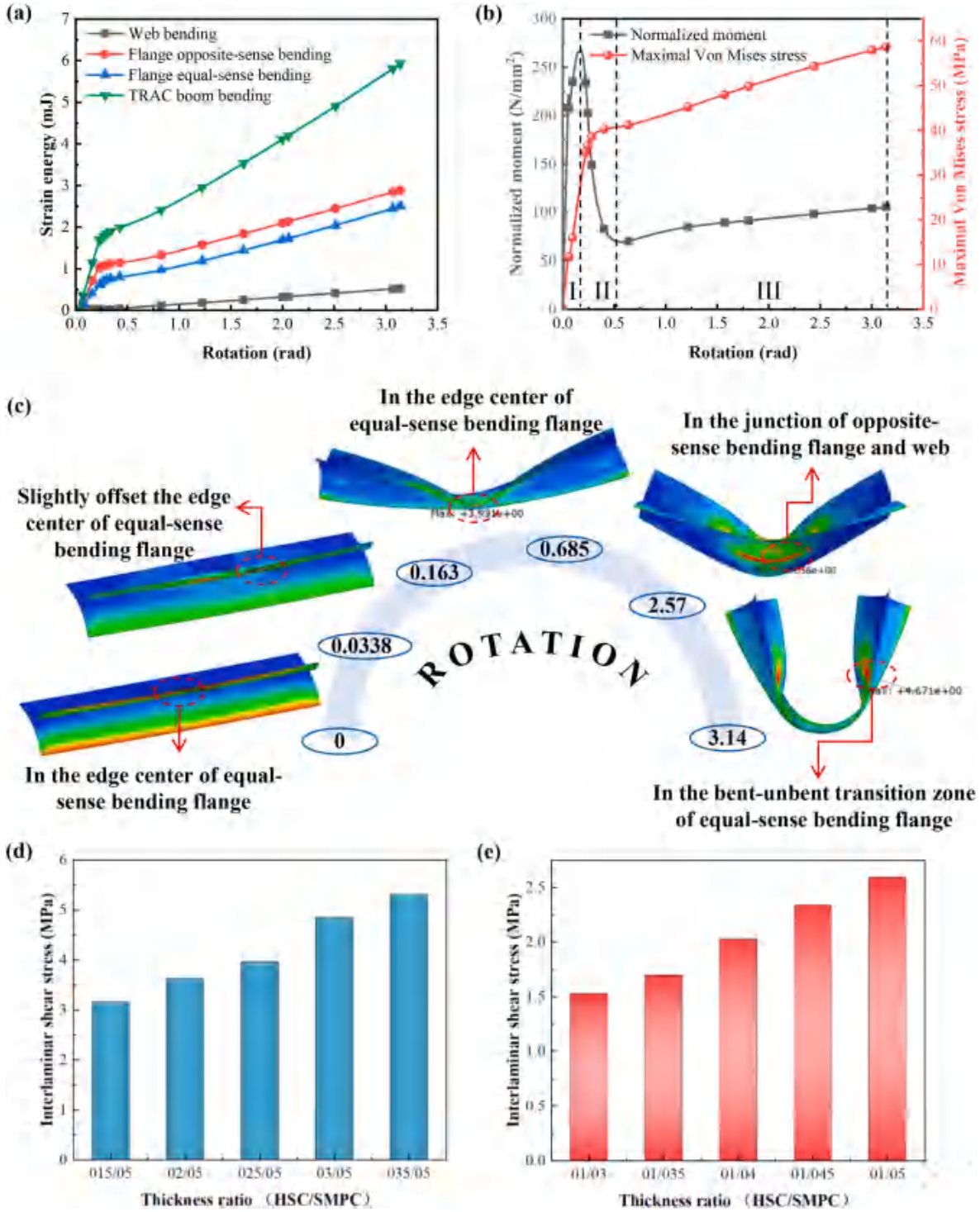

Fig. 10. Bending behavior of the TRAC boom, (a) strain energy, (b) normalized moment and maximal Von Mises stress versus rotation curves, (c) deformation and stress distribution, the peak simulated $\tau_{IL,FE}$ with a fixed (d) SMPC thickness and (e) HSC thickness, the numeric labels represent the layer thicknesses of the HSC and SMPC in hundredths of a millimeter (e.g., 015 corresponds to 0.15 mm).

conducted at 125 °C. The specimens underwent five continuous loading-unloading cycles at a 16:1 span-to-thickness ratio up to a flexural strain of 5%. As illustrated in Fig. 8(f), the force deflection curves exhibit a pronounced hysteresis loop. This phenomenon originates from the inherent thermoviscoelasticity of the polymer matrix near T_g, where energy is dissipated due to internal molecular friction during chain segment rearrangement. Notably, while an initial softening is observed after the first cycle, the hysteresis loops and peak loads become increasingly consistent, reaching a stable state by the fifth cycle. No interfacial delamination was observed after the test, demonstrating the excellent fatigue resistance and interfacial durability of the hybrid composite under repeated thermomechanical loading.

2.4. Computational shape memory behavior

A finite element model was developed using ABAQUS/Standard to simulate stress distribution, deformation patterns, and shape memory behavior during folding and deployable process. A model with a dimension of transverse curvature radius $R = 10$ mm, opening angle $\theta = 60°$, web segment width $w = 5$ mm, length $L = 60$ mm was established in Fig. 9. These dimensions were established to align with the specific envelope requirements of a target flight demonstration mission. Specifically, the radius R and length L were constrained by the volumetric limitations of the dispenser to ensure compact stowage. The web width w was configured to provide a geometric transition zone between the flanges, effectively alleviating stress concentrations at the root during the high strain flattening and coiling process. Crucially, the opening angle θ was selected through a parametric trade-off study and finalized at 60° to balance conflicting design requirements. While a larger angle theoretically increases the stored strain energy and recovery moment, it proportionally expands the flattened width. Consequently, the selected configuration represents an optimal design point that generates sufficient driving force for reliable deployment while ensuring the flattened structure remains within the allowable stowage envelope. It incorporated laminated configurations where the thicknesses of HSC and SMPC layers were systematically varied to regulate structural performance. The numerical framework employed 3D shell elements (S4R type), meshed via “Structured” technique to generate 24960 elements. Rotational constraints were applied at both ends of the boom. A four-step “Visco” analysis was implemented with geometric nonlinearity opened.

High-temperature deformation (125 °C): programmable bending curvature;

Cooling under load (125 °C → 25 °C): freezing temporary shape;

Low-temperature unloading (25 °C): releasing external constraints;

Heating recovery (25 °C → 125 °C): thermally induced shape memory recovery, of which includes free recovery for evaluating shape recovery ratios and constrained recovery for quantifying recovery moments.

To accurately capture the time- and temperature-dependent behavior of the SMPC, a linear viscoelastic constitutive model based on the generalized Maxwell model was adopted. The stress relaxation modulus $E(t)$, is represented by a Prony series expansion:

$$E(t) = E_\infty + \sum_{i=1}^{n} E_i \exp\left(-\frac{t}{\tau_i}\right) \tag{16}$$

where E_∞ is the equilibrium modulus, E_i represents the relaxation modulus of the i-th Maxwell element, and τ_i is the corresponding relaxation time. Temperature dependence is incorporated using the time-temperature superposition principle. The shift factor α_T, which relates the relaxation times at a specific temperature T to those at a reference temperature T_{ref}, is governed by the Williams-Landel-Ferry (WLF) equation:

$$log(\alpha_T) = \frac{-C_1 (T - T_{ref})}{C_2 + (T - T_{ref})} \tag{17}$$

where C_1 and C_2 are material constants determined from experimental characterization. In the ABAQUS implementation, the reduced time $\xi(t)$ is calculated as:

$$\xi(t) = \int_0^t \frac{dt'}{\alpha_T(T(t'))} \tag{18}$$

The Prony series parameters (E_i, τ_i) were identified by fitting a Prony series to the storage modulus master curve constructed from DMA data via the time-temperature superposition principle. The WLF parameters (C_1, C_2) were obtained by fitting the corresponding shift factors used for master curve construction, consistent with the methodology in Ref. [36].

The fitted model reproduces the master curve behavior over the time scales and temperature range relevant to the deployment analyses. In addition, temperature dependent tensile tests were performed and used to validate the model predictions under monotonic loading. It is noted that the present formulation is linear viscoelastic, and the nonlinear features in the structural recovery response are mainly associated with large deformation kinematics. The fitted model reproduces the master curve behavior over the time-temperature domain of interest for the subsequent simulations. A potential concern is time-dependent stress relaxation of the HSC during high temperature coiling, which could reduce long-term elastic energy storage. In the present protocol, the programming temperature is 125 °C, which is well below the viscoelastic transition region of the HSC. This indicates that the HSC response during programming is predominantly elastic over the relevant time scale, supporting the elastic representation of the HSC adopted in the finite element model. Long duration stress relaxation characterization will be addressed in future work to quantify time effects beyond the current experimental time scales.

2.4.1. Bending behavior

The bending strain energy of web, equal-sense and opposite-sense bending flanges, as well as the TRAC boom system are compared in Fig. 10 (a). The strain energies continue to increase with the rotation angle. The web region exhibits the lowest strain energy, showing a nearly linear growth. In contrast, the flange regions store significantly higher strain energy, with the opposite-sense bending flange notably greater than that of the equal-sense bending region. The energy in flanges increases rapidly initially, and its growth rate decreases when the rotation angle reaches 0.29 rad. Similarly, the overall energy of the TRAC boom demonstrates a significant increase, growing from 0 to 0.29 rad, following by a modest increase from 0.29 rad to 3.14 rad. For pure bending, the relationship between curvature κ and the applied moment M is governed by the material's flexural rigidity according to classical beam theory:

$$M = \kappa EI \tag{19}$$

where E is the elastic modulus and I is the area moment of inertia. For a beam with a rectangular cross section, the moment of inertia is given by:

$$I = \frac{BH^3}{12} \tag{20}$$

where B is the width and H is the thickness. Consequently, to eliminate the influence of specimen thickness on the bending moment, we normalize the moment by the cube of the thickness. As shown in Fig. 10 (b), the bending process can be divided into three stages according to the change of bending moment with rotation. In the first stage, the moment increases almost linearly from 0 to 42.78 N/mm^2 with the rotation angle from 0 to 0.18 rad. In the second stage, the moment decreases with the increase of the rotation angle due to energy loss. When the rotation angle increases to 0.57 rad, it drops to 11.05 N/mm^2. In the third stage,

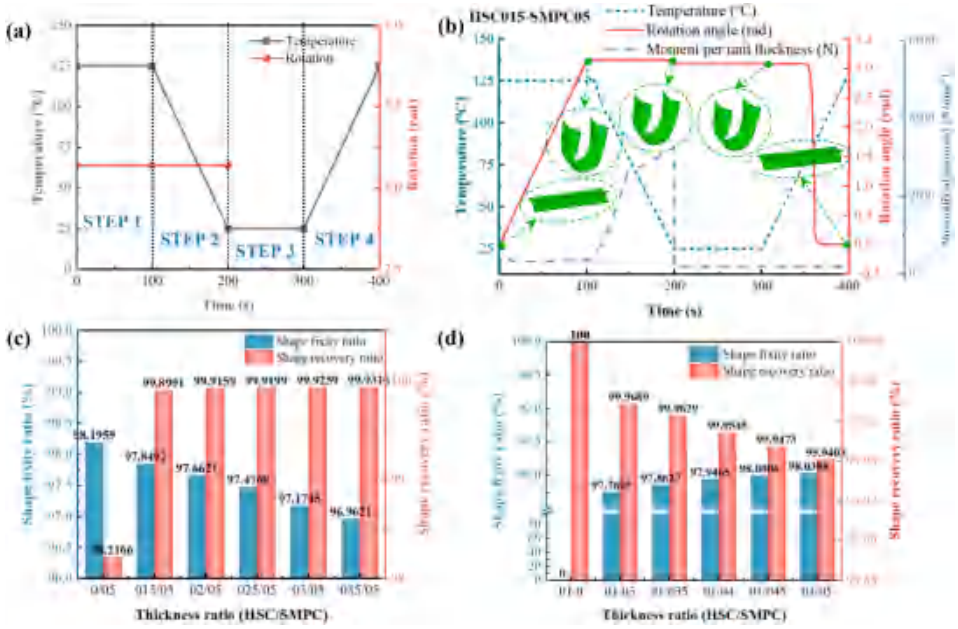

Fig. 11. Free recovery, (a) loading conditions, (b) temperature, rotation and normalized moment variations, shape fixity and recovery ratios with a fixed (c) SMPC thickness and (d) HSC thickness, the numeric labels represent the layer thicknesses of the HSC and SMPC in hundredths of a millimeter (e.g., 015 corresponds to 0.15 mm).

the moment climbs with the rotation angle until it reaches 16.92 N/mm^2 when the boom is fully folded. The maximal Von Mises stress exhibits a consistent increasing trend with the rotation angle, and its increasing rate decreases significantly beyond 0.33 rad. Meanwhile, the location of the maximal stress in Fig. 10(c) shifts continuously throughout the deformation process. During the rotation from 0 to 0.0338 rad, the maximal stress initially emerges in the edge center of the equal-sense bending flange. It subsequently propagates toward both sides of the edge until the rotation reaches 0.163 rad. It returns to the center until 0.685 rad. As the rotation angle further increases to 2.57 rad, the maximal stress shifts to the junction of the opposite-sense bending flange and web. Finally, within the angle range of 2.57 to 3.14 rad, it settles within the bent-unbent transition zone of the equal-sense bending flange.

To enable a consistent comparison with the ILSS obtained from SBS testing, an apparent interlaminar shear stress was extracted from the laminated shell finite element results. The transverse shear per unit width was computed from the shell section force components as:

$$Q = \sqrt{SF4^2 + SF5^2} \tag{21}$$

and converted by thickness normalization:

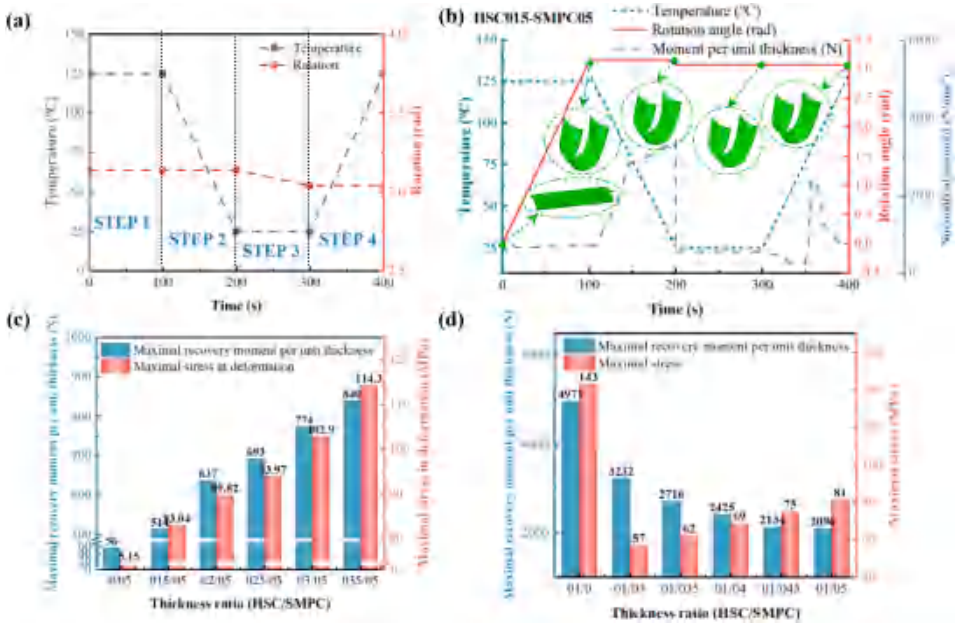

Fig. 12. Constrained displacement recovery, (a) loading conditions, (b) temperature, rotation and normalized moment variations, maximal normalized recovery moment and Von Mises stress in deformation with a fixed (c) SMPC thickness and (d) HSC thickness, the numeric labels represent the layer thicknesses of the HSC and SMPC in hundredths of a millimeter (e.g., 015 corresponds to 0.15 mm).

$$\tau_{IL,FE} = \frac{Q}{t} \tag{22}$$

where t is the total laminate thickness. Since the SBS method provides an engineering measure of interlaminar shear resistance rather than a pointwise interface traction, $\tau_{IL,FE}$ is used here as a comparable stress metric for correlation with the measured ILSS. Two thickness ratio sweeps were carried out to quantify the peak apparent interlaminar shear stress. As shown in Fig. 10(d), when the SMPC thickness was held constant and the HSC thickness was increased, the peak $\tau_{IL,FE}$ rose monotonically from approximately 3.1 MPa to 5.32 MPa as the ratio changed from 0.15/0.05 to 0.35/0.05. Similarly, with the HSC thickness fixed and the SMPC thickness increased, the peak $\tau_{IL,FE}$ increased steadily from about 1.5 MPa to about 2.6 MPa over the investigated ratios in Fig. 10(e). These results consistently indicate that increasing the total laminate thickness increases the transverse shear demand and therefore elevates $\tau_{IL,FE}$. Notably, the maximum simulated $\tau_{IL,FE}$ is 5.32 MPa, which is 42.87% of the experimentally measured ILSS at the operating temperature of 125 °C. This provides a clear margin against shear driven interfacial failure under the investigated thermomechanical deployment conditions and supports the perfectly bonded interface assumption in the present finite element model.

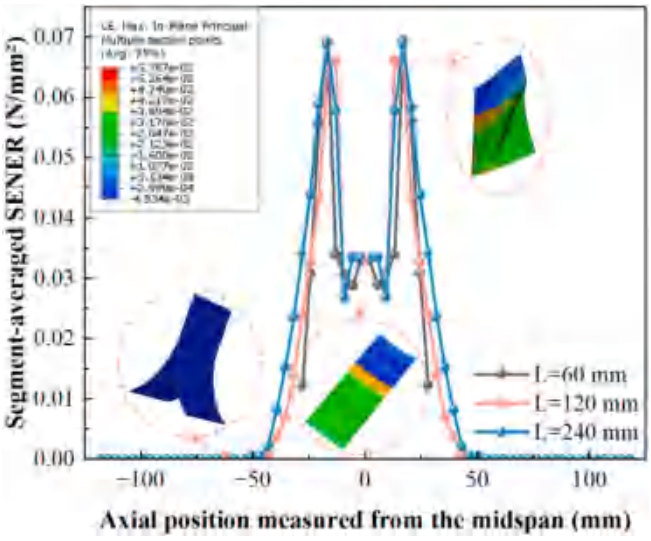

Fig. 13. Strain energy density (SENER) along the boom axis at the end of programming for L = 60, 120, and 240 mm.

2.4.2. Free recovery

Thermo-mechanical loading conditions in free recovery simulation are shown in Fig. 11(a), where a rotational displacement of 3.14 rad was prescribed in the first two steps, followed by unloading in the subsequent two steps. The time period for each step was set to 100 s, with both heating and cooling applied as linear ramps. As shown in Fig. 11(b), the thermo-mechanical cycle consists of four steps. In the first step, the temperature is 125 °C, while the rotational displacement is linearly increased from 0 to 3.14 rad. The moment rises sharply during the initial stage, followed by a rapid decrease until reaching a plateau. Step two involves a linear temperature decrease to 25 °C under a fixed rotational constraint. The cooling induced stiffening of the material prompts a rapid rise in the moment, which then slows down substantially thereafter. In the third step, the rotational constraint is removed at 25 °C, resulting in a partial reduction in rotation due to elastic recovery, and the moment drops to zero upon unloading. Finally, in the fourth step, the temperature is increased again. The shape recovery begins at approximately 85 °C and almost completes by 125 °C. The shape fixity ratio R_f can be calculated as:

$$R_f = \frac{\theta_3}{\theta_1} \times 100\% \tag{17}$$

The shape recovery ratio R_r is expressed as:

$$R_r = \frac{\theta_4 - \theta_3}{0 - \theta_3} \times 100\% \tag{18}$$

where θ_1, θ_3 and θ_4 denote the rotation angle in every step.

To provide quantitative baselines, pure SMPC (0/05) and pure HSC (01/0) cases were included in Fig. 11(c and d) for comparison with the hybrid configurations. Because HSC was simplified as a purely elastic material in the simulation, it yields $R_f = 0$ and $R_r = 100\%$. These values are reported only as a baseline under the adopted metric and do not represent a shape memory response. Two thickness ratio sweeps were performed: one with a fixed SMPC thickness of 0.5 mm and varying HSC thickness, and the other with a fixed HSC thickness of 0.1 mm and varying SMPC thickness. With increasing HSC thickness at fixed SMPC thickness in Fig. 11(c), the shape fixity decreases slightly from 97.85% to 96.96%, while the recovery ratio increases marginally from 99.90% to 99.93%. This indicates that increasing the elastic contribution promotes springback upon unloading, reducing fixity while slightly enhancing recovery. When the HSC thickness is fixed at 0.1 mm and the SMPC thickness increases in Fig. 11(d), the shape fixity improves from 97.76% to 98.03%, while the recovery ratio decreases slightly from 99.97% to 99.94%. This reflects improved temporary shape fixation with higher SMPC content, at the expense of a minor reduction in recovery ratio. Compared with pure SMPC, adding HSC slightly improves recovery while retaining high fixity. Compared with pure HSC, adding SMPC enables temporary shape fixation.

2.4.3. Constrained displacement recovery

Thermo-mechanical loading conditions applied in constrained displacement recovery simulation are presented in Fig. 12(a). A rotational displacement of 3.14 rad was imposed in the first two steps. In the fourth step, the displacement constraint corresponded to the fixed rotation of the unloaded shape obtained in the third step of the free recovery simulation. All other parameters remained consistent with those used in the free recovery case. The shape memory behavior under constrained displacement conditions is illustrated in Fig. 12(b). In contrast to the free recovery case, constrained displacement recovery prevents the structure from returning to its original shape, and the recovery tendency is therefore manifested as a measurable reaction moment whose sign follows the adopted moment convention. The results in the first three steps follow the same trend as in the free recovery case. In the fourth step, as the temperature increases, a slight negative moment initially arises because thermally induced strain develops before the shape memory recovery strain becomes significant. Under the imposed displacement constraint, the resulting reaction moment can therefore oppose the defined positive direction. Subsequently, when the temperature reaches approximately 76 °C, the moment reverses and becomes positive, increasing rapidly. This reversal occurs because the shape memory driven recovery strain becomes dominant over the thermally induced strain contribution under the same constraint. It peaks around 90 °C, then declines sharply before the rate of decrease gradually slows, eventually stabilizing at a value approximately one tenth of the maximum.

The constrained displacement recovery was also investigated under two thickness variations, consistent with the free recovery. For reference, the pure SMPC case (0/05) exhibits a recovery moment per unit thickness of 56 N/mm^2 and a stress of 5.15 MPa, whereas the pure HSC case (01/0) exhibits 4971 N/mm^2 and 143 MPa, respectively. In the first case with fixed SMPC and varying HSC thicknesses shown in Fig. 12(c), the recovery moment per unit thickness increases from 56 N/mm^2 (0/05) to 840 N/mm^2 (035/05), and the stress increases from 5.15 MPa to 114.3 MPa. In the second case with fixed HSC and varying SMPC thicknesses shown in Fig. 12(d), the recovery moment per unit thickness

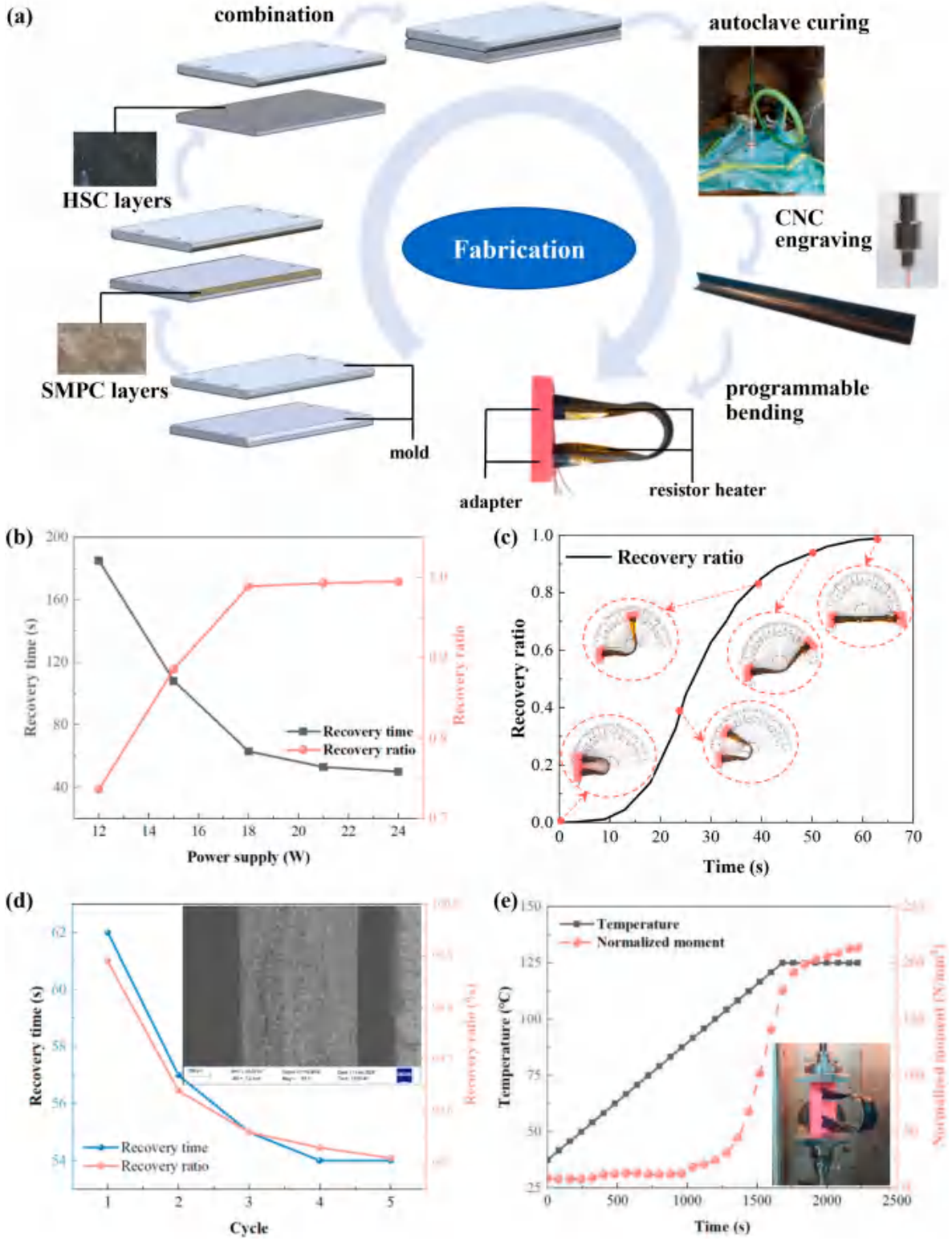

Fig. 14. Experimental shape memory performance, (a) fabrication, (b) recovery time and ratio versus power supply,(c) free recovery process, (d) recovery time and ratio versus cyclic times, (e) constraint displacement recovery.

decreases from 4971 N/mm^2 (01/0) to 2134 N/mm^2 (01/045), while the stress decreases markedly from 143 MPa (01/0) to 57 MPa (01/03) and then increases gradually to 62 MPa (01/035), 69 MPa (01/04), and 75 MPa (01/045) as the SMPC thickness further increases. Compared with the pure HSC case (01/0), introducing SMPC significantly reduces the peak stress, which is beneficial for large deformation deployment. However, with the HSC thickness fixed, further increasing the SMPC thickness leads to a moderate stress increase while the recovery moment continues to decrease.

A length scaling analysis was performed to examine whether the stored energy becomes spatially nonuniform as the TRAC boom is scaled up. Geometrically similar models with identical laminate architecture

were analyzed at lengths of 60, 120, and 240 mm while maintaining the same programmed curvature and boundary conditions. The stored energy distribution at the end of the programming step was quantified using the strain energy density output SENER. As shown in Fig. 13, all three lengths exhibit the same characteristic distribution pattern. Two pronounced peaks appear near the transitions between the flattened bending region and the straight region, indicating that energy concentration is governed primarily by geometric transition zones. The central region shows a lower energy level, which is attributed to local curvature redistribution during programming, as also suggested by the deformation contours. Outside the programmed region, SENER approaches zero, consistent with negligible deformation.

2.5. Experimental shape memory performance

The samples were fabricated using a vacuum-assisted molding process, as illustrated in Fig. 14(a). A two-part mold with curved edges was designed for the TRAC configuration. The manufacturing process involved the following steps. First, fiber fabrics cut to the designed dimensions were manually placed in the curved edge region, and SMP resin was applied via hand lay-up to form SMPC layers. Subsequently, a basalt-aramid prepreg was laid over the mold surface to form the HSC layer. The fabric orientation was set to a $\pm 45^{\circ}$ angle with respect to the boom axis based on the criterion of promoting shear dominated, recoverable deformation during thermomechanical programming and subsequent recovery. Adjacent plies were stacked with alternating yarn directions (AF/BF in the first ply and BF/AF in the second ply) to mitigate directional bias and reduce anisotropy driven coupling in the laminate response. The resulting layer thicknesses were governed by the reinforcement architecture. The HSC layer was constrained to a single prepreg ply to minimize the flattening strain ratio, resulting in a nominal cured thickness of $t_1 = 0.25$ mm. Conversely, the SMPC layer thickness was determined to be $t_2 = 0.5$ mm, dictated by the 3-ply reinforcement schedule. The mold was then closed and transferred to an autoclave for curing. The curing cycle was conducted under a pressure of 0.3 MPa with a heating rate of 2 °C/min, including dwell stages of 3 h at 80 °C, 3 h at 100 °C, and 5 h at 150 °C. After demolding, the booms were precisely cut using a CNC engraving machine and pre-bent into a folded configuration. To facilitate accurate measurement of angular change during free recovery and to ensure reliable contact with the compression plates in constrained displacement recovery, adapters were designed and fabricated via 3D printing method. The present fabrication was adopted for laboratory prototyping to ensure consolidation quality and geometric fidelity. Scale-up will require dedicated tooling and tighter process control to maintain uniform thickness and fiber placement along longer components. Consistency was monitored using cured thickness and mass checks, together with post-demolding visual inspection. A batch-level statistical assessment of variability and quantitative defect inspection will be addressed in future work.

Deployment is triggered by active electrothermal actuation rather than passive solar heating. A flexible resistor heater, shown in Fig. 14(a), was bonded to the boom surface and powered by an external supply to raise the laminate above the T_g of the SMPC, thereby initiating free recovery. This active approach enables commanded and repeatable deployment, which is required for satellite operation. Heater actuation is flight relevant, but it can produce temperature gradients along the boom, which partly explains the discrepancy between simulation and experiment because the numerical model assumes a uniform thermal field. Similar nonuniform heating under heater based activation has been reported for space oriented SMPC deployable mechanisms [10,37]. A more uniform environment, such as an environmental chamber [38], could improve agreement with the uniform temperature model, but it is not representative of the intended on orbit activation strategy. To optimize actuation efficiency, the influence of heating power on recovery behavior was investigated in Fig. 14(b). At 12 W, the recovery time is 185 s and the recovery ratio is 73.82%. At 18 W, the recovery time decreases to 63 s and the recovery ratio reaches 99.89%. Increasing the power to 24 W provides only marginal additional improvement. The corresponding electrical energy inputs are approximately 2.22 kJ at 12 W, 1.13 kJ at 18 W, and 1.20 kJ at 24 W. Considering the tight satellite power budget and overall actuation efficiency, 18 W was selected as the optimal heating power because it achieves near complete recovery with the lowest total input energy.

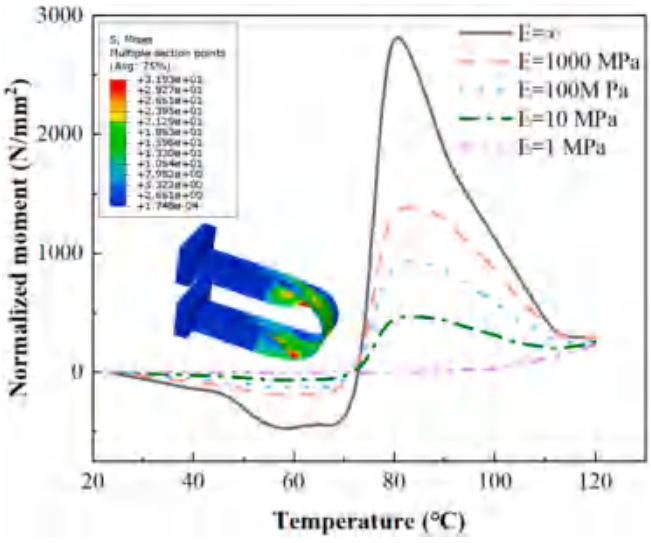

Fig. 15. Influence of adapter stiffness on the simulated normalized recovery moment.

Under the optimized 18 W power supply, the detailed recovery sequence is shown in Fig. 14(c). The deployment initiated approximately 10 s after activation, followed by a rapid increase in the recovery rate. The process decelerated around 40 s and essentially reached completion at 63 s. The experimental recovery ratio of 99.89% aligns closely with the simulated value of 99.91%, with the minor discrepancy likely due to the non uniform temperature field of the heater in practical tests. To address the concern regarding potential functional degradation, the cyclic reliability was assessed through five consecutive folding-deployment sequences in Fig. 14(d). The results demonstrate that the recovery time slightly decreases with the number of cycles, dropping from 63 s in the first cycle to approximately 53 s by the fifth cycle. This trend is attributed to the viscoelastic training effect and a more stabilized internal heat distribution within the hybrid composite layers after initial activation. Crucially, the recovery ratio remained highly stable across all cycles, consistently maintaining values above 99.5%. Together with the stabilized mechanical hysteresis observed in the material level cyclic tests in Fig. 8(f), these system level results confirm that the hybrid TRAC boom possesses excellent fatigue resistance and durable shape memory characteristics, with no observable degradation in its self locking and deployment capabilities under repeated use.

The results of the constrained displacement recovery test are presented in Fig. 14(e). The folded TRAC boom, mounted vertically via its end adapters, was placed between the compression plates of a Zwick/Roell Z010 machine equipped with a temperature chamber. Under a constant displacement condition, the temperature was raised at 2 °C/min to 125 °C and held for 5 min. The variation in load during heating was recorded and used to calculate the recovery moment. The experimental results indicate that the normalized recovery moment began to increase at approximately 85 °C, followed by a rapid rise. As the temperature approached 125 °C, the increase slowed and eventually stabilized at about 215 N/mm^2. A significant discrepancy exists between the experimental recovery moment evolution and the simulation results presented in Fig. 12(b). The experimental curve does not exhibit the rapid rise and subsequent sharp drop predicted by the simulation. However, its final stabilized value agrees well with the simulated steady-

state moment. This divergence primarily stems from differences in boundary conditions. The simulation assumed perfectly fixed constraints, which are highly sensitive to rotational changes, while the experiment utilized 3D-printed porous polylactic acid (PLA) adapters to support the boom during the vertical test configuration. Since the T_g of PLA (approximately 60 °C) is lower than the initiation temperature of the boom's recovery, the adapters soften during heating before the boom begins its recovery. Thus, the initial slight recovery tendency of the boom was accommodated by the deformation of the compliant adapters, which reduces the measured transient peak relative to the perfectly fixed simulation. Accordingly, the experimental response is governed by boundary compliance, which motivates the following stiffness sensitivity analysis.

To further examine the influence of adapter compliance, additional finite element simulations were conducted by explicitly modeling the adapters and varying their elastic modulus from 1 MPa to 1000 MPa, together with an ideal rigid boundary condition. The adapters were connected to the TRAC boom ends using a tie constraint to replicate the experimental constraint configuration. The results shown in Fig. 15 indicate that decreasing adapter stiffness significantly reduces the recovery moment and smooths the transient evolution. This trend is attributed to the finite rotational compliance at the boom ends, which reduces moment transmission compared with an ideal fully fixed constraint. The stiffness sweep provides a sensitivity assessment of the recovery moment evolution, and the predicted response approaches the experimentally observed trend as the adapter modulus decreases. From an engineering perspective, fully fixed constraints are uncommon and recovery typically occurs in a system with finite compliance. Therefore, the stabilized recovery moment at the end of the thermal cycle is adopted as a more practically relevant design parameter than the transient peak under an ideal rigid boundary. This value can be used to evaluate functional requirements that depend on the available steady deployment moment.

The present work focuses on the conceptual design, manufacturing route, interfacial mechanics, and thermomechanical structural validation of the hybrid TRAC boom. Dedicated evaluation under representative space environmental conditions remains a necessary step for future lunar and space deployment. Such testing typically includes ultraviolet irradiation, atomic oxygen exposure, and vacuum thermal cycling. These environmental factors can affect both the polymer matrix and the reinforcing fibers, and therefore may influence long term performance and reliability. Atomic oxygen is widely recognized as a major driver of erosion and performance degradation for organic materials and polymer matrix composites in low Earth orbit, which motivates the adoption of protective strategies for long duration exposure [39]. Aramid fibers are also reported to be susceptible to ultraviolet induced degradation and vulnerable to atomic oxygen attack, whereas inorganic mineral based fibers generally exhibit higher environmental stability [40,41]. Notably, the hybrid is an intraply basalt and aramid architecture rather than an interply stacking sequence. The environmental response should therefore be interpreted as the coupled behavior of the two yarn systems within each ply. In practical missions, deployable polymer matrix composite booms are rarely left bare. They are commonly protected by multilayer insulation blankets and by atomic oxygen resistant surface treatments to mitigate matrix degradation and reduce severe thermal gradients [42,43]. Future work will include representative space environment testing and protective integration to further assess long term durability.

3. Conclusions

This study presents a novel hybrid TRAC boom fabricated by integrating a high strain composite layer with a shape memory polymer composite layer. This design synergistically combines the benefits of both material systems. The SMPC layer provides thermally triggered self locking and shape recovery functions, while the HSC layer serves as an effective elastic energy reservoir, significantly enhancing the recovery moment. Experimental results demonstrate that the hybrid configuration retains excellent shape memory performance while substantially increasing the recovery moment. Individual HSC and SMPC specimens have been fabricated and characterized through dynamic mechanical analysis as well as tensile and flexural tests. The results indicate that the SMPC exhibits a more pronounced stiffness reduction with increasing temperature and a higher failure strain compared to the HSC. The basalt-aramid fabric reinforced composites exhibited excellent mechanical properties along the basalt fiber direction and better toughness along the aramid fiber direction, highlighting its suitability for relevant applications and an ISRU-informed design perspective by increasing the fraction of mineral-based reinforcement. Although differences existed between the simulated and measured recovery moment curves, mainly due to different boundary conditions, the final steady state moment is reproduced with good agreement. This stabilized moment is a practically relevant metric for engineering applications under compliant boundary conditions. This work validates the hybrid design as a reliable approach for developing self deploying space structures that require substantial actuation moment and controlled deployment.

Future research will focus on refining the constitutive model, investigating the interfacial properties between the composite layers, and optimizing the layup design for specific mission requirements. In addition, representative space environment evaluations, including ultraviolet irradiation, atomic oxygen exposure, and vacuum thermal cycling, will be pursued to further assess long-term durability.

CRediT authorship contribution statement

Dou Zhang: Writing – original draft, Project administration, Methodology, Funding acquisition, Formal analysis, Conceptualization. **Changyu Shan:** Validation, Data curation. **Fengfeng Li:** Writing – review & editing, Funding acquisition. **Peidong Liu:** Conceptualization. **Yin Xing:** Data curation. **Xin Lan:** Writing – review & editing, Funding acquisition. **Genyang Cao:** Resources. **Liwu Liu:** Resources, Project administration. **Yanju Liu:** Supervision, Resources. **Jinsong Leng:** Supervision, Resources.

Declaration of competing interest

The authors declare the following financial interests/personal relationships which may be considered as potential competing interests: Dou Zhang reports financial support was provided by National Natural Science Foundation of China. Fengfeng Li reports financial support was provided by National Natural Science Foundation of China. Xin Lan reports financial support was provided by National Natural Science Foundation of China. If there are other authors, they declare that they have no known competing financial interests or personal relationships that could have appeared to influence the work reported in this paper.

Acknowledgments

This work is supported by the National Natural Science Foundation of China (Grant Nos: 12402403, 12102107 and 12272113).

Data availability

Data will be made available on request.

References

[1] Wang B, Zhu J, Zhong S, Liang W, Guan C. Space deployable mechanics: a review of structures and smart driving. Mater Des 2024;237:112557. https://doi.org/10.1016/j.matdes.2023.112557.
[2] Zhang X, Nie R, Chen Y, He B. Deployable structures: structural design and static/dynamic analysis. J Elasticity 2021;146:199–235. https://doi.org/10.1007/s10659-021-09860-6.

[3] Ma X, An N, Cong Q, Bai J-B, Wu M, Xu Y, et al. Design, modeling, and manufacturing of high strain composites for space deployable structures. Commun Eng 2024;3:78. https://doi.org/10.1038/s44172-024-00223-2.
[4] Chuang S, Huawei C, Hongwei G, Rongqiang L, Dezheng Y, Hongjuan J, et al. Design and driving optimization of a space-towed deployable arm. Eng Struct 2023;278:115540. https://doi.org/10.1016/j.engstruct.2022.115540.
[5] Pellegrino S. Large retractable appendages in spacecraft. J Spacecraft Rockets 1995;32:1006–14. https://doi.org/10.2514/3.26722.
[6] Murugesan S. An overview of electric motors for space applications. IEEE Trans Ind Electron Control Instrum 1981;IECI-28:260–5. https://doi.org/10.1109/TIECI.1981.351050.
[7] Luo L, Zhang F, Wang L, Liu Y, Leng J. Recent advances in shape memory polymers: multifunctional materials, multiscale structures, and applications. Adv Funct Mater 2024;34:2312036. https://doi.org/10.1002/adfm.202312036.
[8] Yadav A, Singh SK, Das S, Kumar S, Kumar A. Shape memory polymer and composites for space applications: a review. Polym Compos 2025;46:11647–83. https://doi.org/10.1002/pc.29707.
[9] Lan X, Liu L, Zhang F, Liu Z, Wang L, Li Q, et al. World's first spaceflight on-orbit demonstration of a flexible solar array system based on shape memory polymer composites. Sci China Technol Sci 2020;63:1436–51. https://doi.org/10.1007/s11431-020-1681-0.
[10] Zhang D, Liu L, Xu P, Zhao Y, Li Q, Lan X, et al. World's first application of a self-deployable mechanism based on shape memory polymer composites in Mars explorations: ground-based validation and on-mars qualification. Smart Mater Struct 2022;31:115008. https://doi.org/10.1088/1361-665X/ac93d1.
[11] Zeng C, Liu L, Du Y, Yu M, Xin X, Liu T, et al. A shape-memory deployable subsystem with a large folding ratio in China's tianwen-1 mars exploration mission. Engineering 2023;28:49–57. https://doi.org/10.1016/j.eng.2023.01.005.
[12] Lan X, Liu Y, Lv H, Wang X, Leng J, Du S. Fiber reinforced shape-memory polymer composite and its application in a deployable Hinge. Smart Mater Struct 2009;18:24002. https://doi.org/10.1088/0964-1726/18/2/024002.
[13] Wang C, Wang Y. The mechanical design of a hybrid intelligent Hinge with shape memory polymer and spring sheet. Composites Part B 2018;134:1–8. https://doi.org/10.1016/j.compositesb.2017.09.039.
[14] Li F, Liu L, Lan X, Wang T, Li X, Chen F, et al. Modal analyses of deployable truss structures based on shape memory polymer composites. Int J Appl Mech 2016;8:1640009. https://doi.org/10.1142/S1758825116400093.
[15] Li F, Liu L, Du L, Liu Y, Leng J. Mechanical analysis of a tip-loaded deployable truss based on shape memory polymer composite. Compos Struct 2020;242:112196. https://doi.org/10.1016/j.compstruct.2020.112196.
[16] Ming G, Liu L, Liu Y, Leng J. Space deployable parabolic reflector based on shape memory polymer composites. Compos Struct 2023;304:116327. https://doi.org/10.1016/j.compstruct.2022.116327.
[17] Rahmatabadi D, Soleyman E, Fallah Min Bashi M, Aberoumand M, Soltanmohammadi K, Ghasemi I, et al. 4D printing and annealing of PETG composites reinforced with short carbon fibers. Phys Scripta 2024;99:055957. https://doi.org/10.1088/1402-4896/ad3b40.
[18] Rahmatabadi D, Aberoumand M, Soltanmohammadi K, Soleyman E, Ghasemi I, Baniassadi M, et al. A new strategy for achieving shape memory effects in 4D printed two-layer composite structures. Polymers 2022;14. https://doi.org/10.3390/polym14245446.
[19] Mirasadi K, Yousefi MA, Jin L, Rahmatabadi D, Baniassadi M, Liao W-H, et al. 4D printing of magnetically responsive shape memory polymers: toward sustainable solutions in soft robotics, Wearables, and Biomedical Devices n.d. https://doi.org/10.1002/advs.202513091.
[20] Bayati A, Rahmatabadi D, Khajepour M, Baniassadi M, Abrinia K, Bodaghi M, et al. 4D printing of composite thermoplastic elastomers for super-stretchable soft artificial muscles n.d. https://doi.org/10.1002/app.57177.
[21] Rahmatabadi D, Yousefi MA, Shamsolhodaei S, Baniassadi M, Abrinia K, Bodaghi M, et al. 4D printing of polyethylene glycol-grafted carbon nanotube-reinforced polyvinyl chloride–polycaprolactone composites for enhanced shape recovery and thermomechanical performance n.d. https://doi.org/10.1002/aisy.202500113.
[22] Ye W-Q, Fu W-X, Liu X-P, Yang C-G, Xu Z-R. A shape-reconfigurable, light and magnetic dual-responsive shape-memory micropillar array chip for droplet manipulation. Chin Chem Lett 2024;35:108494. https://doi.org/10.1016/j.cclet.2023.108494.
[23] Lv C, Zhou Z, Li Y, Lu S, Bai Y. Multi-responsive shape memory porous composites for self-powered sensors and self-sensing actuators. Chem Eng J 2023;477:147059. https://doi.org/10.1016/j.cej.2023.147059.
[24] Zhou Z, Bai Y, Niu L, Lv C, Li Y, Niu L. Versatile ionogels with tailoring performance for strain sensors, temperature alarm and self-powered wearable devices. Chem Eng J 2024;488:150982. https://doi.org/10.1016/j.cej.2024.150982.
[25] Hu X, Zhao W, Zhang Z, Xie J, He J, Cao J, et al. Novel 3D printed shape-memory PLLA-TMC/GA-TMC scaffolds for bone tissue engineering with the improved mechanical properties and degradability. Chin Chem Lett 2023;34:107451. https://doi.org/10.1016/j.cclet.2022.04.049.
[26] Liang X, Niu L, Song J, Chen Z, Qu H, Wen D, et al. Fatigue-resistant, self-healing and antibacterial poly(ionic liquid) gel multichannel sensors for underwater early warning and deep learning-assisted infant monitoring. Chem Eng J 2025;526:170881. https://doi.org/10.1016/j.cej.2025.170881.
[27] Shi Y, Cooper CB, Nogusa T, Lai J-C, Lyu H, Khatib M, et al. Shape-memory-assisted self-healing of macroscopic punctures via high-energy-density periodic dynamic polymers with tunable actuation temperature. Matter 2024;7:2108–24. https://doi.org/10.1016/j.matt.2024.03.013.
[28] Lan X, Hao S, Liu L, Liu Y, Leng J. Macroscale bending large-deformation and microbuckling behavior of a unidirectional fiber-reinforced soft composite. J Compos Mater 2020;54:243–57. https://doi.org/10.1177/0021998319854145.
[29] Liu Z, Lan X, Bian W, Liu L, Li Q, Liu Y, et al. Design, material properties and performances of a smart Hinge based on shape memory polymer composites. Composites Part B 2020;193:108056. https://doi.org/10.1016/j.compositesb.2020.108056.
[30] Echter MA, Silver MJ, D'Elia E, Peterson M, Reid BM. Recent developments in precision high strain composite hinges for deployable space telescopes. 2018 AIAA spacecr. Struct. Conf., American Institute of Aeronautics and Astronautics; n.d. https://doi.org/10.2514/6.2018-0939.
[31] Davis B, Turse D, Francis WH. The deployment of large de-orbit sails utilizing high strain composite booms. AIAA Scitech 2019 forum, American Institute of Aeronautics and Astronautics; n.d. https://doi.org/10.2514/6.2019-1750.
[32] Maji AK, Harris M, Garcia D, deBlonk BJ. Feasibility assessment of deployable composite telescope. J Aero Eng 2011;24:12–9. https://doi.org/10.1061/(ASCE)AS.1943-5525.0000045.
[33] Chamberlain MK, Kiefer SH, LaPointe M, LaCorte P. On-orbit flight testing of the roll-out solar array. Acta Astronaut 2021;179:407–14. https://doi.org/10.1016/j.actaastro.2020.10.024.
[34] Çelik O, Yaşar A, Karaçor B. Properties of basalt/aramid fiber reinforced hybrid composites compared to carbon fiber composites. Polym Compos 2023;44:3509–21. https://doi.org/10.1002/pc.27339.
[35] Liu T, Liu L, Yu M, Li Q, Zeng C, Lan X, et al. Integrative Hinge based on shape memory polymer composites: material, design, properties and application. Compos Struct 2018;206:164–76. https://doi.org/10.1016/j.compstruct.2018.08.041.
[36] Chen J, Liu L, Liu Y, Leng J. Thermoviscoelastic shape memory behavior for epoxy-shape memory polymer. Smart Mater Struct 2014;23:055025. https://doi.org/10.1088/0964-1726/23/5/055025.
[37] Zhang D, Liu L, Xu P, Zhao Y, Li Q, Lan X, et al. Ancient papyrus scroll-inspired self-deployable mechanism based on shape memory polymer composites for Mars explorations. Compos Struct 2023;304:116391. https://doi.org/10.1016/j.compstruct.2022.116391.
[38] Zhang D, Liu L, Lan X, Leng J, Liu Y. Synchronous deployed design concept triggered by carbon fibre reinforced shape memory polymer composites. Compos Struct 2022;290:115513. https://doi.org/10.1016/j.compstruct.2022.115513.
[39] Verker R, Keren E, Refaeli N, Carmiel Y, Bolker A, David D, et al. Measurements of material erosion in space by atomic oxygen using the on-orbit material degradation detector. Acta Astronaut 2023;211:818–26. https://doi.org/10.1016/j.actaastro.2023.07.020.
[40] Xu Y, Zhang H, Huang G. Review on the mechanical deterioration mechanism of aramid fabric under harsh environmental conditions. Polym Test 2023;128:108227. https://doi.org/10.1016/j.polymertesting.2023.108227.
[41] Zhiyao LI, Kun YaN, Wenwen W, Qinghua Z, Dong W, Chenguang Y. Effects of ultraviolet irradiation on the structure and properties of aramid fibers. J Radiat Res Radiat Process 2024;42:30201. https://doi.org/10.11889/j.1000-3436.2024-0001.
[42] Singh D, Singh MK, Chaubey A, Ganguly AK, Singh V. Thermal performance improvement of multilayer insulation technique. Heat Mass Tran 2023;59:1365–78. https://doi.org/10.1007/s00231-022-03330-y.
[43] Yan C, Li J, Dai Y, Lan Z, Wang H, Tong H, et al. Fabrication of high-performance ALD-Al2O3/SiO2 nanolaminate coating for atomic oxygen erosion resistance on polyimide. Surf Coat Technol 2025;502:131960. https://doi.org/10.1016/j.surfcoat.2025.131960.